

Implicit Neural Representation-Based Continuous Single Image Super Resolution: An Empirical Study

Tayyab Nasir

The University of Western Australia

tayyabnasir22@gmail.com, tayyab.nasir@research.uwa.edu.au

Daochang Liu

The University of Western Australia

daochang.liu@uwa.edu.au

Ajmal Mian

The University of Western Australia

ajmal.mian@uwa.edu.au

Abstract

Implicit neural representation (INR) has become the standard approach for arbitrary-scale image super-resolution (ASSR). To date, no empirical study has systematically examined the effectiveness of existing methods, nor investigated the effects of different training recipes, such as scaling laws, objective design, and optimization strategies. A rigorous empirical analysis is essential not only for benchmarking performance and revealing true gains but also for establishing the current state of ASSR, identifying saturation limits, and highlighting promising directions. We fill this gap by comparing existing techniques across diverse settings and presenting aggregated performance results on multiple image quality metrics. We contribute a unified framework and code repository¹ to facilitate reproducible comparisons. Furthermore, we investigate the impact of carefully controlled training configurations on perceptual image quality and examine a new loss function that penalizes intensity variations while preserving edges, textures, and finer details during training. We conclude the following key insights that have been previously overlooked: (1) Recent, more complex INR methods provide only marginal improvements over earlier methods. (2) Model performance is strongly correlated to training configurations, a factor overlooked in prior works. (3) The proposed loss enhances texture fi-

delity across architectures, emphasizing the role of objective design for targeted perceptual gains. (4) Scaling laws apply to INR-based ASSR, confirming predictable gains with increased model complexity and data diversity.

1 Introduction

Single-image super resolution (SISR) is the process of converting a low-resolution image into a higher resolution one [1, 2, 3, 4]. In its simplest form, such a process deals only with creating a fixed-scale version of the image, usually upscaling by an integer scale. Arbitrary scale, or continuous, super-resolution can generate a higher-resolution image of any size, using non-integer scaling factors [5, 6, 7]. Implicit neural representation methods have gained significant attention for continuous image super-resolution, as their ability to map continuous signal coordinates directly to RGB values of higher resolution provides a simple and flexible way of training [8, 9, 10]. This paper focuses on continuous image super-resolution using INR-based methods, providing a detailed empirical analysis of the existing techniques.

MetaSR [11] and LIIF [12] are two of the earliest methods that used INR-based techniques for continuous single-image super-resolution, where the former uses it as an upscaling module, while the latter defines an encoder-decoder INR-architecture. The encoder’s job is to generate a latent feature map in spatial dimensions from the

¹Code available at: <https://github.com/tayyabnasir22/INR-ASSR-Empirical-Analysis>

input low-resolution image. Conventionally, fixed SISR models are used as an encoder [13, 14]. The generated latent code is queried using the desired higher resolution coordinates. The resultant latent feature vectors, along with additional scale information, are passed to the decoder to get the RGB values for each of the input coordinates. Additional components are also used within the same architecture [12], such as feature unfolding to enhance the quality of information encoded in the latent representations, cell decoding to represent the target scale information, and local ensembling averaging over neighboring coordinates.

Techniques like LTE [12], SRNO [7], CLIT [15], CiaoSR [16], and HIIIF [17] follow the aforementioned architecture. Each technique, as reported in prior research, compares its performance with the predecessor in a semi-controlled experimental setting, using the same datasets and scaling factors, with Peak Signal to Noise Ratio (PSNR) as the primary evaluation metric. However, a lack of transparency in the reproducibility of results and fair benchmarking remains problematic, as newer studies do not replicate prior results under comparable settings.² For example, some studies use a larger patch size of 128^2 and the Stochastic Gradient Descent with Warm Restarts (SGDR) [18] for training, rather than the 48^2 patch and multi-step training scheduler used in prior studies. Hence, it remains unclear whether the reported improvements reflect true architectural improvements or are largely due to differences in training strategies, and whether the earlier techniques, being simpler, can perform well compared to the newer, more complex works, under similar settings.

Another limitation lies in the lack of diverse image quality assessment (IQA), with most studies relying solely on PSNR, thereby offering a limited perspective on perceptual image quality. Validation PSNR is often used to select the best model weights in each study, introducing further bias in comparative evaluations. Moreover, the impact of different training recipes on targeted perceptual improvements for INR-based ASSR remains unexplored. These issues are largely overlooked in prior works and continue to pose a significant bottleneck to further advancement in this area.

To address the lack of consistency in training and evaluation of existing techniques and introduce a general transparency in comparisons, we conduct extensive experiments, using diverse but consistent settings for training

and evaluation. Specifically, we trained 6 ASSR methods using 6 experimental setups and 2 different encoders, and evaluated them across 7 datasets and 7 IQA metrics. Furthermore, we provide a centralized code repository for easy reproducibility and comparison. Additionally, we investigate the impact of different learning strategies on performance by evaluating existing training recipes and introducing a new loss function, demonstrating the potential for achieving targeted perceptual quality improvements under carefully designed training settings. Finally, we present a comprehensive set of analyses, addressing the aforementioned questions. A summary of our key findings is as follows:

- **Marginal Improvements of Recent Models:** Recent, more complex INR-based ASSR models yield marginal improvements over earlier methods, suggesting that the current architectural designs may have reached a saturation point on existing datasets. The maximum PSNR gain observed in our experiments was merely 0.035 dB for SRNO, the top-performing model, compared to the next best method, further supporting this observation.
- **Sensitivity to Training Configurations:** Performance gains can be attained not only through architectural modifications but also by carefully tuning the training configurations and optimization settings. For example, HIIIF shows a strong dependency on the learning rate scheduler. Hence, reproducing prior work under new training settings is essential for a fair comparison.
- **Sensitivity to Perceptual Objectives:** Different architectures show varying performance trends across IQA metrics. Moreover, targeted training objectives aimed at specific perceptual objectives present a promising direction for achieving further progress in INR-based super-resolution. This fact is solidified by the improved texture fidelity achieved by the proposed loss function over the standard L1 loss.
- **Effect of Scaling Laws:** Scaling laws generally hold for INR-based ASSR methods, where an increase in model parameters generally correlates with improved performance across different IQA metrics. However, the rate of improvement diminishes as

complexity grows, indicating a saturation point in parameter-driven gains. Similarly, training using additional compute and more diverse data correlates with model performance.

In summary, we provide a long-awaited empirical analysis to consolidate existing efforts and pave the way for future studies on ASSR. Our main contributions include:

1. We present a comprehensive analysis and a systematic audit of existing INR-based continuous image super-resolution for analyzing the effects of different training strategies, including variations in scaling laws, optimization schemes, and objective designs.
2. We create a single code repository for a centralized, systematic benchmarking framework to ensure fair evaluations and facilitate research extensions.
3. We achieve targeted perceptual improvements for existing architectures through our newly proposed hybrid pixel-gradient loss, combining L1-loss with first-order derivatives, which enhances texture fidelity in alignment with our empirical findings.

2 Related work

Image Super Resolution (SISR): SRCNN [19] was the first method that used a deep neural network architecture for SISR, proposing a fully convolutional neural network. SRCNN inspired a series of shallow and deep CNN-based architectures for SISR [20, 21, 22, 23, 24]. Recently, attention [25, 2], diffusion [26, 27], and state space model (SSM) [28, 29, 30] based techniques have also been proposed for SISR. However, many of these architectures rely on components such as deconvolution [23] or sub-pixel convolutions [24], which constrain the upsampling process to fixed integer scales, limiting their flexibility for continuous-scale image reconstruction [31, 15].

Arbitrary-Scale Super-Resolution (ASSR) extends conventional SISR by enabling upscaling by any non-integer factor, making it a more practical and flexible solution for real-world applications. VDSR [20] is among the first methods for ASSR, employing a pre-upsampling strategy, resizing the input image to the desired scale using bicubic upsampling, followed by a CNN that reconstructs the high-frequency details. Subsequent attempts,

such as OverNet [32], EQSR [33], and SRWarp [34], further explore pre-upsampling and warping-based strategies. A detailed discussion of these approaches is presented in the survey [5].

Implicit Neural Representation (INR): Over the years, INR has emerged as the most popular approach for ASSR, owing to its simplicity and flexibility. INR utilizes a multi-layer perception (MLP) for mapping input coordinates to a continuous signal [8]. It has been widely used for 3D tasks, such as 3D scene reconstruction, 3D image compression, and 3D object shape modeling [35, 9, 36, 6, 37]. MetaSR [11] was the first to use coordinate and scale information for ASSR, introducing a meta-upscale module that dynamically generates convolutional weights to produce high-resolution images. LIIF [6] introduced an MLP-based local implicit function to predict RGB values for queried coordinates, proposing the first encoder-decoder architecture for INR-based ASSR, serving as the basis for later methods, including LTE [12], SRNO [7], CiaoSR [16], CLIT [15], and HIIF [17]. Additional architectural components, such as feature unfolding and local ensemble mechanisms, are also used in INR-based architecture for ASSR [6]. LTE proposed changes for improving fine detail reconstruction by transforming coordinates into the Fourier domain before feeding them into the implicit decoder. CiaoSR and CLIT introduced the use of attention for context-aware feature encoding for the query coordinates, while SRNO uses Galerkin attention to capture non-local spatial dependencies more efficiently. HIIF introduced hierarchical positional encoding to represent local features and coordinates across multiple scales.

Training and Evaluation Objectives: Different objectives have been applied for learning and evaluating super-resolution techniques. L1-loss is the most commonly used loss for ASSR, particularly in INR-based methods, as summarized in Table 1. However, it has a limited ability to reconstruct high-frequency details. Alternate objective functions targeting perceptual reconstruction have also been explored. Perceptual losses [38] compute the Euclidean distance between high-level features extracted from a pretrained network for the ground truth and generated images, encouraging perceptual similarity. In this category, texture losses, often based on Gram matrix [39], promote consistency in texture and structural details. Similarly, mixed losses combine L1-loss with per-

ceptual or texture loss, aiming to balance pixel-level accuracy with perceptual fidelity.

PSNR is the most widely used metric for evaluating super-resolution methods. While it strictly measures pixel-level intensity differences, it does not capture perceptual similarity. More perception-oriented metrics include SSIM [40], which evaluates luminance, contrast, and structural similarity, and LPIPS [41], which leverages deep neural network features to quantify perceptual similarity between image patches. LPIPS generally aligns more closely with human perception of image quality than PSNR. Nevertheless, despite its limitations, PSNR remains the primary evaluation metric, particularly for INR-based ASSR methods, limiting the assessment of perceptual performance.

3 Method

Our proposed unified experimental framework systematically and consistently evaluates INR-based ASSR methods across diverse settings. It provides a consistent performance-ranking protocol across a comprehensive set of evaluation metrics and datasets, presents a targeted analysis of perceptual improvement gains from tuned objectives, and examines the effects of scaling laws.

3.1 Datasets

Following prior works, we used the DIV2K [42] dataset for training, which consists of 800 high-quality 2K-resolution images for training and 100 images for validation. For testing, we used Set5 [43], Set14 [44], BSD100 [45], and Urban100 [46] datasets, along with SVT [47] and CelebA-HQ [48] for diverse domain-specific evaluations given in Appendix. The combined test sets are denoted as D .

3.2 Empirical Experiment Settings

Methods and Configurations: We conducted comprehensive experiments on existing INR-based methods, including MetaSR, LIIF, LTE, SRNO, CiaoSR, and HIIIF. This set of techniques constitutes the model set M . Another related work CLIT [15], was excluded from the empirical analysis due to its substantial complexity, where

it has 15x more parameters compared to the baseline, and employs a much more complex cascaded training strategy. However, its reported performance remains comparable to that of simpler architectures such as CiaoSR, SRNO, and HIIIF [16, 7, 17].

Training Details: All models were trained for 150 epochs to keep the analysis computationally manageable. The reduced training duration does not compromise the convergence, where the detailed convergence plots across different models and training settings are provided in the Appendix, confirming that all models reached stability well before 150 epochs. Table 1 presents a comparison between the training and evaluation settings adopted in prior work and those used in our unified framework. Our framework has a broader and more diverse set of training recipes, denoted as T , along with comprehensive evaluation criteria, enabling a more consistent and thorough assessment of the performance of each method.

Experimental Coverage and Evaluations: We conducted a total of 72 experiments, covering 6 techniques, 2 encoder variants [13, 14], and 6 training recipes. Validation PSNR was tracked during training, and both the best and the 150-epoch model weights were retained for aggregate performance analysis. Performance of each technique was evaluated across multiple datasets and scales using seven IQA metrics, including PSNR, SSIM [40], GMSD [49], FSIM [50], VIF [51], SR-SIM [52], and LPIPS [41], which together define the evaluation set Q .

3.3 Aggregated Ranking Framework

We propose a fair ranking algorithm based on Borda count [53] to provide an aggregated view of each model’s performance across different scales, datasets, IQA metrics, and training recipes. For ranking at the level of individual training recipes, let $V_m^{d,s,q}$ denote the value-rank of model $m \in M$ evaluated on dataset $d \in D$, scale $s \in S$, and IQA metric $q \in Q$, where a higher value-rank indicates better performance. The Borda count for model m is defined as:

$$B_m = \sum_d^D \sum_s^S \sum_q^Q V_m^{d,s,q}. \quad (1)$$

The corresponding aggregated ranking r_m for each model is then computed as:

Recipe Name	Model	Loss	Patch Size	Scale Range	LR Scheduler	Batch Size	Reported IQA
L1-Loss SGDR Larger Patch Larger Scale Gradient Loss Gram-L1-Loss	MetaSR	L1-Loss	50	1-4	Multi-Step	16	PSNR, SSIM
	LIIF	L1-Loss	48	1-4	Multi-Step	16	PSNR
	LTE	L1-Loss	48	1-4	Multi-Step	16	PSNR
	SRNO	L1-Loss	128	1-4	SGDR	64	PSNR
	CiaoSR	L1-Loss	48	1-4	Multi-Step	16	PSNR, SSIM, LPIPS
	HIIF	L1-Loss	48	1-4	SGDR	16	PSNR
MetaSR, LIIF, LTE, SRNO, CiaoSR, HIIF		L1-Loss	48	1-4	Multi-Step		
		L1-Loss	48	1-4	SGDR		
		L1-Loss	64	1-4	Multi-Step	32 for EDSR,	PSNR, SSIM, GMSD,
		L1-Loss	64	1-6	Multi-Step	16 for RDN	FSIM, VIF, SR-SIM,
		Gradient Loss	48	1-4	Multi-Step		LPIPS
		Gram-L1 Loss	48	1-4	Multi-Step		

Table 1: Comparison of training configurations between prior ASSR methods (top) and our unified experimental framework (bottom). The last six rows detail our standardized training recipes T , which combine different loss designs, scale ranges, and schedulers for comprehensive evaluation across multiple IQA metrics.

$$r_m = \text{rank}_{\text{desc}}(B_m). \quad (2)$$

where $r_m \in \mathbb{N}$ denotes the rank of model m , and $R_M = \{r_m | m \in M\}$ represents the complete ranking of all models, with a lower value indicating superior overall performance. Similarly, to obtain rankings based on individual IQA metrics, we define $V_m^{d,s,t}$, where $t \in T$ represents the training recipe, and apply the same Borda count aggregation procedure to compute the ranks. Finally, we use $V_m^{d,s,q,t}$ with the same aggregation procedure, incorporating all datasets, scales, metrics, and training recipes, to obtain the comprehensive global model ranking.

3.4 Hybrid Pixel-Gradient Loss

As part of exploring the impact of targeted training configurations on improving specific perceptual feature quality, we explore a hybrid loss function. This loss combines the pixel-wise L1 error with a first-order gradient consistency term to better preserve local edge structures and texture sharpness during reconstruction. For the ground truth and predicted images, I and \hat{I} , the hybrid loss is defined as:

$$\mathcal{L} = \lambda_{L1}\mathcal{L}_{L1} + \lambda_{grad}\mathcal{L}_{grad}, \quad (3)$$

where

$$\mathcal{L}_{L1} = \|\hat{I} - I\|_1, \quad (4)$$

$$\mathcal{L}_{grad} = \|\nabla_x \hat{I} - \nabla_x I\|_1 + \|\nabla_y \hat{I} - \nabla_y I\|_1. \quad (5)$$

λ_{L1} and λ_{grad} represent the contribution of each term in the final loss, and are set to 1 and 0.05, respectively, in our experiments.

4 Results and Analysis

4.1 Marginal Improvements

Figure 1 presents a detailed comparison of the best results achieved by each model across all different evaluation metrics for the DIV2K validation set, using the EDSR encoder. For this comparison, we selected the best-performing instance of each model from among its differently trained versions to ensure a fair representation of its true performance. The results indicate that while the recent methods have steadily progressed and introduced valuable architectural improvements, the overall performance gains across different scales are marginal. This indicates that the INR-based ASSR architectures have matured considerably on existing benchmarks, suggesting that future advancements will require more innovative and disruptive architectural advancements, as well as more diverse and challenging datasets.

4.2 Sensitivity to Training Configurations

To evaluate the robustness of each model under diverse training configurations, we present Figure 2 with an aggregated analysis to summarize the consistency and stability of different techniques across varying conditions.

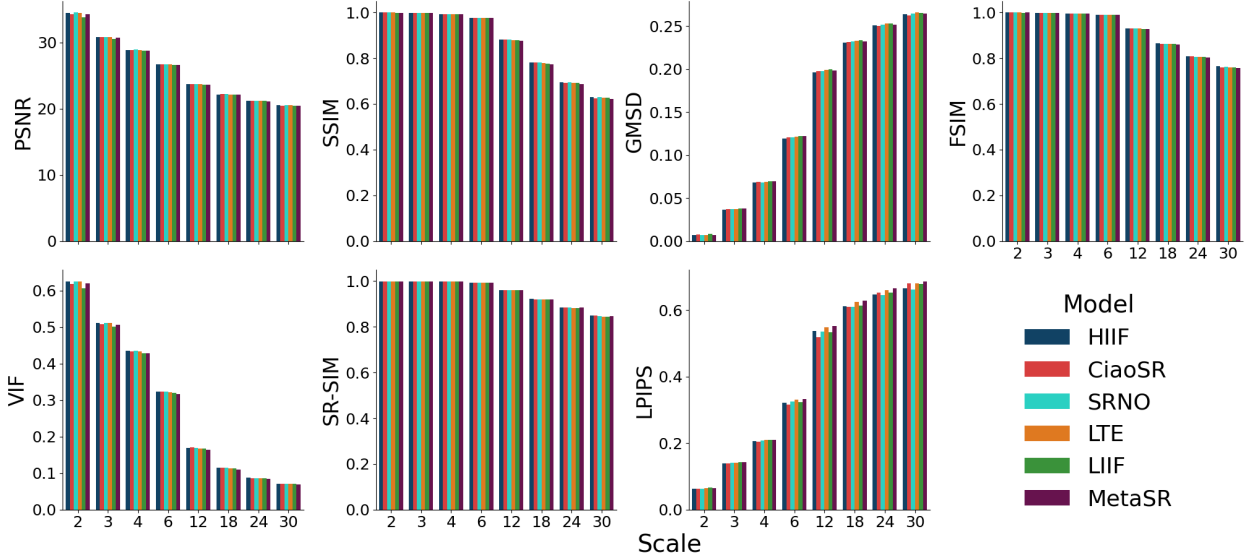


Figure 1: Comparison of best results achieved by different models on the DIV2K dataset across different scaling factors. The x-axis corresponds to the scaling factors, while the y-axis shows the image quality assessment (IQA) values for the different techniques. On all the scales, only marginal performance differences are observed across architectural variations.

We used the Borda aggregation framework defined in Section 3.3 to get the aggregated ranking, computed across the six training settings using the value-rank $V_m^{d,s,q}$, separately for each encoder. Additionally, Figure 2 reports the global rank assigned to each technique, which is shown at the right end of the figure, along with reporting the number of model parameters, excluding those of the encoder. A more detailed breakdown of the results is provided in the Appendix.

The fact that different models excel under different configurations highlights the sensitivity of specific architectures to particular training strategies, emphasizing the need for fair and consistent experimental comparisons. The key takeaways from this analysis suggest that even earlier, simpler models can outperform more recent approaches when trained under appropriately tuned settings. To further investigate this behavior, we provide a detailed analysis of the following two specific training factors:

Impact of Learning Rate Scheduler: Firstly, Fig. 3a) presents a delta plot reporting the change in performance for each model when switching from a multi-step learn-

ing rate scheduler, which decays the learning rate at fixed intervals, to an SGDR scheduler [18]. Although all the techniques show a general improvement under the SGDR or cosine annealing scheduler, HIIF shows the most significant gain. This aligns with prior reports [17], where HIIF's superior performance was achieved using the cosine annealing learning rate scheduling strategy. However, the fact that other models also benefit from this updated scheduler reinforces the importance of conducting fair comparisons under fixed training settings.

Impact of Input Patch Size: Fig. 3b) shows a delta plot reporting the change in performance when switching from an input patch size of 48^2 to 64^2 . There is a general trend of improvement when the patch size is increased, suggesting that increasing the patch size can be beneficial. However, this behavior should be regarded as a general trend, as there is no evidence suggesting that the improvement is significantly beneficial for a particular architecture.

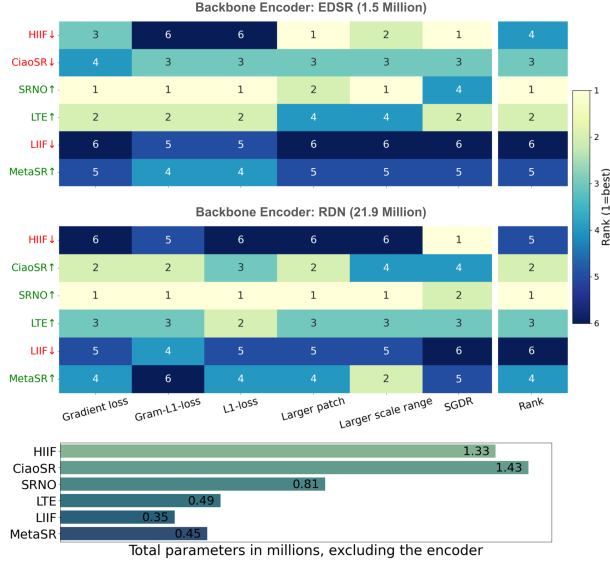


Figure 2: Models ranked based on aggregated performance across datasets, scales, and seven IQA metrics using Borda count aggregation, where lower ranks indicate better overall performance. Ranking variations highlight the sensitivity of different techniques to training configurations. The final rank for each method is shown on the far right, and red downward arrows indicate a drop in rank compared to previously reported results [17].

4.3 Sensitivity to Perceptual Objectives

Impact of IQA Metrics on Model Rankings: Figure 4 provides an aggregated overview of each technique’s performance across different IQA metrics, based on the Borda aggregation framework 3.3. It summarizes each architecture’s sensitivity to both perceptual and non-perceptual quality measures, using the value-rank $V_m^{d,s,t}$. The figure shows that different techniques exhibit varying rankings across the IQA metrics, indicating each architecture’s sensitivity to specific perceptual characteristics. As summarized in Table 1, most prior works have evaluated performance using PSNR alone, which limits the understanding of the perceptual trade-offs. Incorporating a wider range of IQA metrics enables a more balanced and comprehensive evaluation, providing deeper insight into how different architectures optimize structural accuracy and perceptual realism.

Impact of Training Objective on Targeted Perceptual Improvements: We analyze the role of objective design and its influence on targeted perceptual gains. To this end, we analyzed all the models to assess how modifications to the loss function influence their ability to capture improved texture fidelity. Fig. 5 shows the changes in four texture-sensitive IQA metrics when the loss function is modified from L1-loss to more texture-preserving losses, the L1 + Gram loss, and the proposed hybrid pixel-gradient loss. Overall, the metrics indicate positive responses to the modified objectives, with the proposed hybrid gradient loss showing the most consistent improvements across all models. Figure 6 provides a qualitative assessment supporting this observation, showing improved texture fidelity that is evident from the sharper edges and distinct corner structures in the resulting super-resolved images.

Impact of Gradient Weighing Term on Texture Fidelity: The previously discussed targeted texture enhancement via changing the training objective is further investigated by increasing the weighting of the loss term responsible for texture fidelity. For this analysis, we use the SRNO [7] model trained under identical settings, with the gradient consistency term’s weight incrementally raised to 0.075, 0.1, and 0.3. The first part of the Figure 7 maps the IQA metrics related to intensity differences, luminance, contrast, and structural similarity, while the second part maps texture-sensitive metrics. Increasing the gradient weight improves texture sharpness up to a certain threshold; beyond this point, the dominant gradient term begins to interfere with the L1 component’s ability to capture pixel-level intensity, resulting in a decline in PSNR and overall reconstruction quality.

4.4 Scaling Laws Analysis

We investigate the following three aspects of scaling laws to understand their impact on INR-based ASSR.

Model Complexity: We analyze the impact of model complexity by replacing the EDSR [13] encoder, which contains 1.5 million parameters, with the more complex RDN [14] encoder having 21.9 million parameters. Fig. 3c) presents the change in different IQA metrics under identical training settings, showing a general improvement in performance when moving to the higher-capacity encoder.

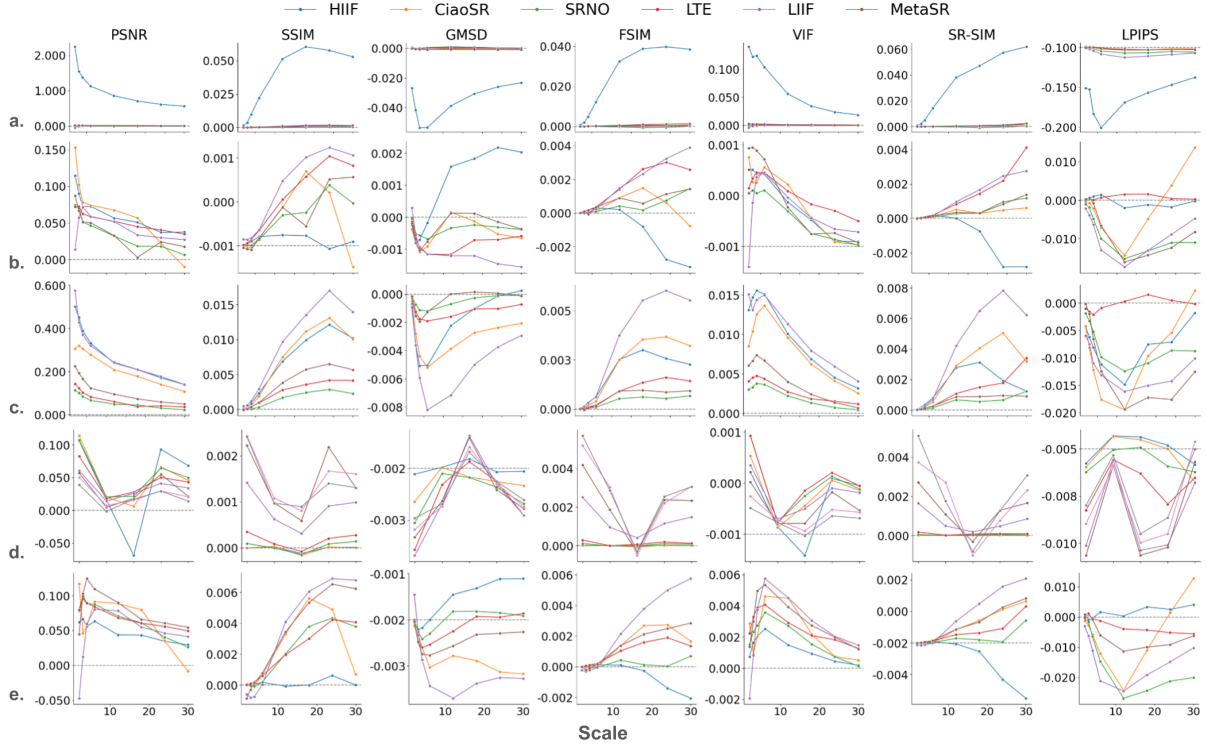


Figure 3: Vertical axis, in each case, is the change in the IQA metric due to a change in training configuration. **a)** Replacing the multi-step learning rate scheduler with SGDR improves performance across all IQA metrics for all techniques, with HIIIF showing the most significant gain. **b)** Increasing the training patch size from 48^2 to 64^2 positively impacts performance across all IQA metrics. **c)** Increasing model complexity by switching the encoder from EDSR (1.5M parameters) to RDN (21.9M parameters) yields improvements consistent with model scaling trends. **d)** Extending training from 100 to 150 epochs shows performance gains consistent with training cost scaling trends. **e)** Expanding the training random scale distribution range from 1–4 to 1–6 improves performance, consistent with scaling trends related to data volume and diversity.



Figure 4: Models ranked per IQA metric based on aggregated performance across datasets, scales, and settings using Borda count aggregation. Variations in ranking highlight the sensitivity of different techniques to specific perceptual metrics. The red downward arrows indicate a decrease in rank relative to previously reported results.

Training Duration: Next, we study the impact of training cost by comparing models trained for 100 epochs versus those trained for 150 epochs, keeping all other settings identical. Figure 3d) presents the change in different IQA metrics, where there is a general improvement trend with increasing the epochs.

Data Diversity: Finally, to analyze the impact of training data size and variability, we increase the maximum scaling range for patch sampling from 1-4 to 1-6. This expands the uniform distribution from which patches are drawn, providing more diverse training examples to the models. Figure 3e) shows the resulting changes in IQA metrics under identical settings, revealing a general trend of marginal improvement.

These results indicate that the general scaling laws established for various learning problems also hold for INR-based ASSR models.

5 Conclusion and discussion

In this study, we presented a unifying and comprehensive framework for an empirical analysis of existing INR-based ASSR methods. Specifically, we conducted a diverse set of experiments to investigate the impact of train-

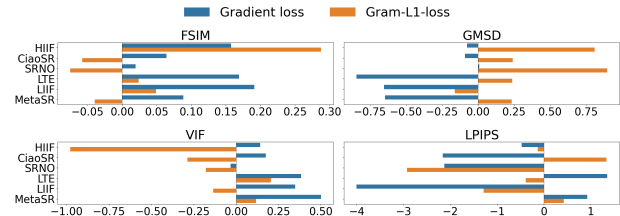


Figure 5: Relative change in texture-sensitive IQA metrics when replacing the L1 loss with L1-Gram and Hybrid-Gradient losses. Overall, the Hybrid-Gradient loss shows consistent performance improvements across architectures.

ing configurations, including variations in objective design, optimization strategies, and scaling laws. We presented a detailed evaluation of existing methods under diverse training settings, utilizing multiple image quality assessment (IQA) metrics, alongside a qualitative assessment of perceptual improvements achieved through targeted training strategies. An aggregated ranking was introduced that identifies the true performance of each architecture across diverse training settings. Finally, we provide a centralized and fully reproducible code repository to support future research extensions and promote transparent, fair comparisons among existing and forthcoming techniques.

The key insights resulting from this empirical study include: 1) Existing INR-based methods have largely stabilized, approaching a saturation point, as reflected by the marginal performance gains observed. 2) Training configurations have a significant impact on model performance and cannot be neglected, as careful tuning can lead to meaningful improvements across architectures. 3) Targeted perceptual improvements can be achieved through focused training, as demonstrated by the proposed loss function improving texture fidelity. Additionally, model architecture choices and carefully controlled training configurations show a strong relationship with performance across different IQA metrics. 4) Scaling laws, previously unexplored for INR-based ASSR, are shown to hold, as demonstrated by performance gains achieved through increased model complexity, training costs, and enhanced training data diversity.

Finally, based on the conducted experiments and anal-

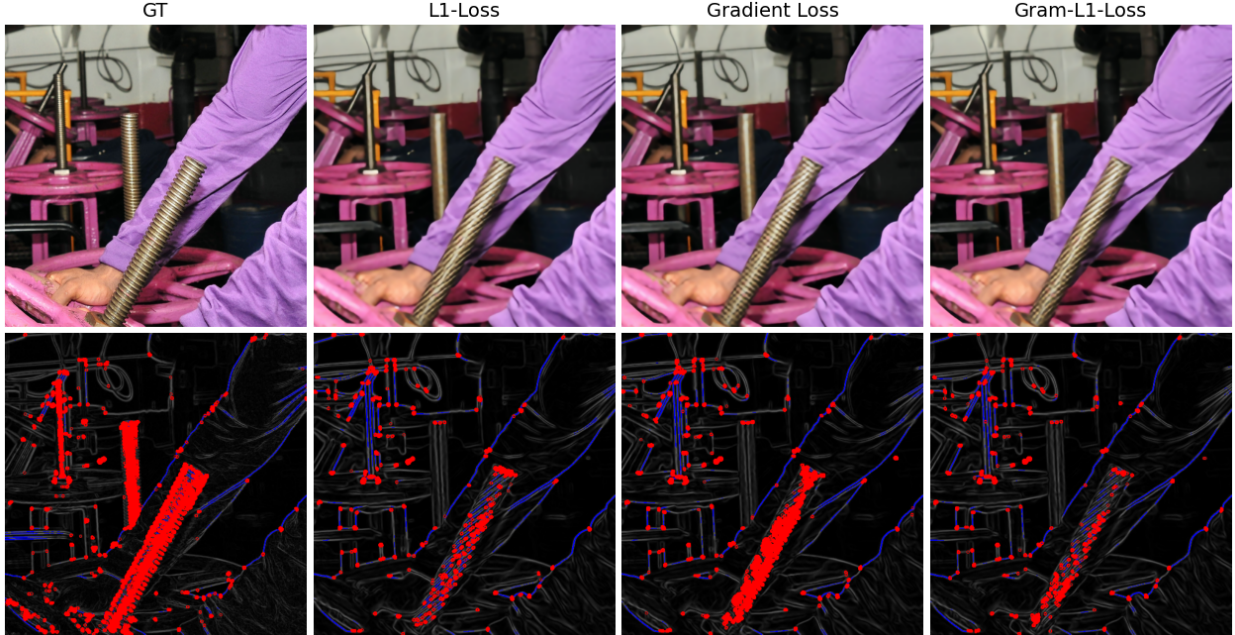


Figure 6: Edge/corner maps for the SRNO model trained with different loss functions on a DIV2K image (5x scaling). The Gradient Loss produces sharper edges (blue-curves) and corners (red-dots), indicating improved texture preservation.

ysis, we identify the following areas for future research:

- **Unified and diverse evaluation benchmarking framework:** Future works can benefit from adopting a unified and diverse benchmarking framework, like the one proposed, that integrates multiple IQA metrics and varied training configurations. This can ensure a more consistent and transparent evaluation for future methods, enabling identification of both general performance trends and model-specific strengths.
- **Need for more complex and diverse benchmark datasets:** The existing architectures reaching a saturation point on the existing benchmarks highlights the need for more comprehensive and diverse datasets. These should include both general and domain-specific collections, annotated for perceptual attributes such as high texture fidelity, consistent colors, strong edge structure, semantic co-

herence, occlusion handling, and depth complexity. Such datasets would complement existing evaluation metrics and provide a stronger basis for evaluating perceptual gains. Furthermore, extending domain-specific datasets beyond faces and real-scene text would enable future work to evaluate indoor versus outdoor environments, photorealistic versus non-photorealistic images, and other specialized domains, providing deeper insights into model generalization and robustness across diverse visual contexts.

- **Targeted perceptual optimization in ASSR:** The exploration of training strategies and architectural designs targeted at achieving specific perceptual gains remains largely underexplored. The empirical findings from our study, particularly those involving the proposed hybrid loss function, demonstrate the potential of such targeted optimization in enhancing perceptual quality. Future studies could focus on

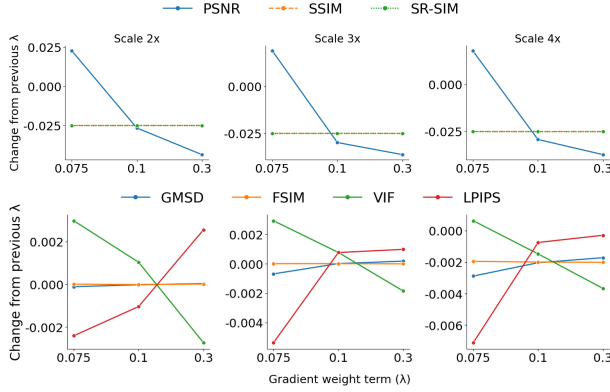


Figure 7: Relative change in various IQA metrics as the weight of the texture fidelity term in the hybrid loss is increased. Results are reported on the DIV2K validation set. The x-axis denotes the updated weight values, while the y-axis shows the change relative to the previous, lower weight.

developing ASSR methods that explicitly target perceptual attributes such as texture fidelity, edge sharpness, and semantic coherence, through refined architectural components and tailored training configurations.

References

- [1] B. B. Moser *et al.*, “Hitchhiker’s guide to super-resolution: Introduction and recent advances,” *IEEE Transactions on Pattern Analysis and Machine Intelligence*, 2023. [1](#)
- [2] B. Niu, W. Wen, W. Ren, X. Zhang, L. Yang, S. Wang, K. Zhang, X. Cao, and H. Shen, “Single image super-resolution via a holistic attention network,” in *European conference on computer vision*. Springer, 2020, pp. 191–207. [1, 3](#)
- [3] B. Moser, A. Shanbhag, F. Raue, S. Frolov, S. Palacio, and A. Dengel, “Diffusion models in image super-resolution and everything: A survey. arxiv,” *arXiv preprint arXiv:2401.00736*, 2024. [1](#)
- [4] Z. Wang, J. Chen, and S. C. Hoi, “Deep learning for image super-resolution: A survey,” *IEEE transactions on pattern analysis and machine intelligence*, 2020. [1](#)
- [5] H. Liu, Z. Li, F. Shang, Y. Liu, L. Wan, W. Feng, and R. Timofte, “Arbitrary-scale super-resolution via deep learning: A comprehensive survey,” *Information Fusion*, vol. 102, p. 102015, 2024. [1, 3](#)
- [6] Y. Chen, S. Liu, and X. Wang, “Learning continuous image representation with local implicit image function,” in *Proceedings of the IEEE/CVF conference on computer vision and pattern recognition*, 2021, pp. 8628–8638. [1, 3](#)
- [7] M. Wei and X. Zhang, “Super-resolution neural operator,” in *Proceedings of the IEEE/CVF Conference on Computer Vision and Pattern Recognition*, 2023, pp. 18247–18256. [1, 2, 3, 4, 7](#)
- [8] B. Mildenhall, P. P. Srinivasan, M. Tancik, J. T. Barron, R. Ramamoorthi, and R. Ng, “Nerf: Representing scenes as neural radiance fields for view synthesis,” *Communications of the ACM*, vol. 65, no. 1, pp. 99–106, 2021. [1, 3](#)
- [9] Z. Chen and H. Zhang, “Learning implicit fields for generative shape modeling,” in *Proceedings of the IEEE/CVF conference on computer vision and pattern recognition*, 2019, pp. 5939–5948. [1, 3](#)
- [10] M. Atzmon and Y. Lipman, “Sal: Sign agnostic learning of shapes from raw data,” in *Proceedings of the IEEE/CVF conference on computer vision and pattern recognition*, 2020, pp. 2565–2574. [1](#)
- [11] X. Hu, H. Mu, X. Zhang, Z. Wang, T. Tan, and J. Sun, “Meta-sr: A magnification-arbitrary network for super-resolution,” in *Proceedings of the IEEE/CVF conference on computer vision and pattern recognition*, 2019, pp. 1575–1584. [1, 3](#)
- [12] J. Lee and K. H. Jin, “Local texture estimator for implicit representation function,” in *Proceedings of the IEEE/CVF conference on computer vision and pattern recognition*, 2022, pp. 1929–1938. [1, 2, 3](#)
- [13] B. Lim, S. Son, H. Kim, S. Nah, and K. Mu Lee, “Enhanced deep residual networks for single image super-resolution,” in *Proceedings of the IEEE conference on computer vision and pattern recognition workshops*, 2017, pp. 136–144. [2, 4, 7, 1](#)
- [14] Y. Zhang, Y. Tian, Y. Kong, B. Zhong, and Y. Fu, “Residual dense network for image super-resolution,” in *Proceedings of the IEEE conference on computer vision and pattern recognition*, 2018, pp. 2472–2481. [2, 4, 7, 1](#)
- [15] H.-W. Chen, Y.-S. Xu, M.-F. Hong, Y.-M. Tsai, H.-K. Kuo, and C.-Y. Lee, “Cascaded local implicit transformer for arbitrary-scale super-resolution,” in *Proceedings of the IEEE/CVF Conference on Computer Vision and Pattern Recognition*, 2023, pp. 18257–18267. [2, 3, 4](#)

[16] J. Cao, Q. Wang, Y. Xian, Y. Li, B. Ni, Z. Pi, K. Zhang, Y. Zhang, R. Timofte, and L. Van Gool, “Ciaosr: Continuous implicit attention-in-attention network for arbitrary-scale image super-resolution,” in *Proceedings of the IEEE/CVF Conference on Computer Vision and Pattern Recognition*, 2023, pp. 1796–1807. [2](#), [3](#), [4](#)

[17] Y. Jiang, H. M. Kwan, T. Peng, G. Gao, F. Zhang, X. Zhu, J. Sole, and D. Bull, “Hiif: Hierarchical encoding based implicit image function for continuous super-resolution,” in *Proceedings of the Computer Vision and Pattern Recognition Conference*, 2025, pp. 2289–2299. [2](#), [3](#), [4](#), [6](#), [7](#), [1](#)

[18] I. Loshchilov and F. Hutter, “Sgdr: Stochastic gradient descent with warm restarts,” *arXiv preprint arXiv:1608.03983*, 2016. [2](#), [6](#)

[19] C. Dong, C. C. Loy, K. He, and X. Tang, “Learning a deep convolutional network for image super-resolution,” in *European conference on computer vision*. Springer, 2014, pp. 184–199. [3](#)

[20] J. Kim, J. K. Lee, and K. M. Lee, “Accurate image super-resolution using very deep convolutional networks,” in *Proceedings of the IEEE conference on computer vision and pattern recognition*, 2016, pp. 1646–1654. [3](#)

[21] K. Zhang, W. Zuo, Y. Chen, D. Meng, and L. Zhang, “Beyond a gaussian denoiser: Residual learning of deep cnn for image denoising,” *IEEE transactions on image processing*, vol. 26, no. 7, pp. 3142–3155, 2017. [3](#)

[22] K. Zhang, W. Zuo, S. Gu, and L. Zhang, “Learning deep cnn denoiser prior for image restoration,” in *Proceedings of the IEEE conference on computer vision and pattern recognition*, 2017, pp. 3929–3938. [3](#)

[23] C. Dong, C. C. Loy, and X. Tang, “Accelerating the super-resolution convolutional neural network,” in *European conference on computer vision*. Springer, 2016, pp. 391–407. [3](#)

[24] W. Shi, J. Caballero, F. Huszár, J. Totz, A. P. Aitken, R. Bishop, D. Rueckert, and Z. Wang, “Real-time single image and video super-resolution using an efficient sub-pixel convolutional neural network,” in *Proceedings of the IEEE conference on computer vision and pattern recognition*, 2016, pp. 1874–1883. [3](#)

[25] T. Dai, J. Cai, Y. Zhang, S.-T. Xia, and L. Zhang, “Second-order attention network for single image super-resolution,” in *Proceedings of the IEEE/CVF conference on computer vision and pattern recognition*, 2019, pp. 11 065–11 074. [3](#)

[26] H. Li, Y. Yang, M. Chang, S. Chen, H. Feng, Z. Xu, Q. Li, and Y. Chen, “Srdiff: Single image super-resolution with diffusion probabilistic models,” *Neurocomputing*, vol. 479, pp. 47–59, 2022. [3](#)

[27] C. Saharia, J. Ho, W. Chan, T. Salimans, D. J. Fleet, and M. Norouzi, “Image super-resolution via iterative refinement,” *IEEE transactions on pattern analysis and machine intelligence*, vol. 45, no. 4, pp. 4713–4726, 2022. [3](#)

[28] H. Guo, J. Li, T. Dai, Z. Ouyang, X. Ren, and S.-T. Xia, “Mambair: A simple baseline for image restoration with state-space model,” in *European conference on computer vision*. Springer, 2024, pp. 222–241. [3](#)

[29] Y. Ren, X. Li, M. Guo, B. Li, S. Zhao, and Z. Chen, “Mambacsr: Dual-interleaved scanning for compressed image super-resolution with ssms,” *arXiv preprint arXiv:2408.11758*, 2024. [3](#)

[30] Y. Shi, B. Xia, X. Jin, X. Wang, T. Zhao, X. Xia, X. Xiao, and W. Yang, “Vmambair: Visual state space model for image restoration,” *IEEE Transactions on Circuits and Systems for Video Technology*, 2025. [3](#)

[31] J.-E. Yao, L.-Y. Tsao, Y.-C. Lo, R. Tseng, C.-C. Chang, and C.-Y. Lee, “Local implicit normalizing flow for arbitrary-scale image super-resolution,” in *Proceedings of the IEEE/CVF Conference on Computer Vision and Pattern Recognition*, 2023, pp. 1776–1785. [3](#)

[32] P. Behjati, P. Rodriguez, A. Mehri, I. Dupont, C. F. Tena, and J. Gonzalez, “Overnet: Lightweight multi-scale super-resolution with overscaling network,” in *Proceedings of the IEEE/CVF Winter Conference on Applications of Computer Vision*, 2021, pp. 2694–2703. [3](#)

[33] X. Wang, X. Chen, B. Ni, H. Wang, Z. Tong, and Y. Liu, “Deep arbitrary-scale image super-resolution via scale-equivariance pursuit,” in *Proceedings of the IEEE/CVF Conference on Computer Vision and Pattern Recognition*, 2023, pp. 1786–1795. [3](#)

[34] S. Son and K. M. Lee, “Srwarf: Generalized image super-resolution under arbitrary transformation,” in *Proceedings of the IEEE/CVF conference on computer vision and pattern recognition*, 2021, pp. 7782–7791. [3](#)

[35] K. Genova, F. Cole, D. Vlasic, A. Sarna, W. T. Freeman, and T. Funkhouser, “Learning shape templates with structured implicit functions,” in *Proceedings of the IEEE/CVF international conference on computer vision*, 2019, pp. 7154–7164. [3](#)

[36] L. Mescheder, M. Oechsle, M. Niemeyer, S. Nowozin, and A. Geiger, “Occupancy networks: Learning 3d reconstruction in function space,” in *Proceedings of the IEEE/CVF conference on computer vision and pattern recognition*, 2019, pp. 4460–4470. [3](#)

[37] S. Klocek, Ł. Maziarka, M. Wołczyk, J. Tabor, J. Nowak, and M. Śmieja, “Hypernetwork functional image representation,” in *International Conference on Artificial Neural Networks*. Springer, 2019, pp. 496–510. [3](#)

[38] J. Johnson, A. Alahi, and L. Fei-Fei, “Perceptual losses for real-time style transfer and super-resolution,” in *European conference on computer vision*. Springer, 2016, pp. 694–711. [3](#)

[39] L. A. Gatys, A. S. Ecker, and M. Bethge, “A neural algorithm of artistic style,” *arXiv preprint arXiv:1508.06576*, 2015. [3](#)

[40] Z. Wang, A. C. Bovik, H. R. Sheikh, and E. P. Simoncelli, “Image quality assessment: from error visibility to structural similarity,” *IEEE transactions on image processing*, vol. 13, no. 4, pp. 600–612, 2004. [4](#)

[41] R. Zhang, P. Isola, A. A. Efros, E. Shechtman, and O. Wang, “The unreasonable effectiveness of deep features as a perceptual metric,” in *Proceedings of the IEEE conference on computer vision and pattern recognition*, 2018, pp. 586–595. [4](#)

[42] E. Agustsson and R. Timofte, “Ntire 2017 challenge on single image super-resolution: Dataset and study,” in *Proceedings of the IEEE conference on computer vision and pattern recognition workshops*, 2017, pp. 126–135. [4](#)

[43] M. Bevilacqua, A. Roumy, C. Guillemot, and M. L. Alberi-Morel, “Low-complexity single-image super-resolution based on nonnegative neighbor embedding,” 2012. [4](#)

[44] R. Zeyde, M. Elad, and M. Protter, “On single image scale-up using sparse-representations,” in *International conference on curves and surfaces*. Springer, 2010, pp. 711–730. [4](#)

[45] D. Martin, C. Fowlkes, D. Tal, and J. Malik, “A database of human segmented natural images and its application to evaluating segmentation algorithms and measuring ecological statistics,” in *Proceedings eighth IEEE international conference on computer vision. ICCV 2001*, vol. 2. IEEE, 2001, pp. 416–423. [4](#)

[46] J.-B. Huang, A. Singh, and N. Ahuja, “Single image super-resolution from transformed self-exemplars,” in *Proceedings of the IEEE conference on computer vision and pattern recognition*, 2015, pp. 5197–5206. [4](#)

[47] K. Wang and S. Belongie, “Word spotting in the wild,” in *European conference on computer vision*. Springer, 2010, pp. 591–604. [4](#)

[48] T. Karras, T. Aila, S. Laine, and J. Lehtinen, “Progressive growing of gans for improved quality, stability, and variation,” *arXiv preprint arXiv:1710.10196*, 2017. [4](#)

[49] W. Xue, L. Zhang, X. Mou, and A. C. Bovik, “Gradient magnitude similarity deviation: A highly efficient perceptual image quality index,” *IEEE transactions on image processing*, vol. 23, no. 2, pp. 684–695, 2013. [4](#)

[50] L. Zhang, L. Zhang, X. Mou, and D. Zhang, “Fsim: A feature similarity index for image quality assessment,” *IEEE transactions on Image Processing*, vol. 20, no. 8, pp. 2378–2386, 2011. [4](#)

[51] H. R. Sheikh and A. C. Bovik, “A visual information fidelity approach to video quality assessment,” in *The first international workshop on video processing and quality metrics for consumer electronics*, vol. 7, no. 2. sn, 2005, pp. 2117–2128. [4](#)

[52] L. Zhang and H. Li, “Sr-sim: A fast and high performance iqia index based on spectral residual,” in *2012 19th IEEE international conference on image processing*. IEEE, 2012, pp. 1473–1476. [4](#)

[53] I. McLean, “The borda and condorcet principles: three medieval applications,” *Social Choice and Welfare*, vol. 7, no. 2, pp. 99–108, 1990. [4](#)

[54] R. M. Haralick, K. Shanmugam, and I. H. Dinstein, “Textural features for image classification,” *IEEE Transactions on systems, man, and cybernetics*, no. 6, pp. 610–621, 2007. [2](#)

[55] Y. Li, Y. Zhang, R. Timofte, L. Van Gool, L. Yu, Y. Li, X. Li, T. Jiang, Q. Wu, M. Han *et al.*, “Ntire 2023 challenge on efficient super-resolution: Methods and results,” in *Proceedings of the IEEE/CVF Conference on Computer Vision and Pattern Recognition*, 2023, pp. 1922–1960. [2](#)

[56] J. Yoo, N. Ahn, and K.-A. Sohn, “Rethinking data augmentation for image super-resolution: A comprehensive analysis and a new strategy,” in *Proceedings of the IEEE/CVF conference on computer vision and pattern recognition*, 2020, pp. 8375–8384. [2](#)

Appendix

Additional details and analysis are presented here:

- Appendix A: Details about experimental settings.
- Appendix B: Detailed qualitative analysis of the proposed hybrid L1-gradient loss function.
- Appendix C: Detailed breakdown of the results presented under diverse settings.

A Experimental setup

A.1 Data preparation

For training, 800 images from DIV2K were processed through a data generator that extracted patches of size 48^2 or 64^2 , depending on the selected configuration. Bicubic downsampling was applied to generate the corresponding low-resolution patches from the high-resolution images, with the target non-integer scaling factor sampled uniformly from a distribution $\mathcal{U}(x, y)$, where $x = 1$ and y was set to 4 or 6 based on the selected training configuration. To further increase data diversity, each patch was randomly augmented through horizontal, vertical, or diagonal flips. Each image was repeated 40 times, with a new combination of random augmentation, patch selection, and scaling factor applied at each repetition, creating a highly varied training set.

For testing, bicubic downsampling was applied to generate low-resolution inputs from the ground-truth high-resolution images of DIV2K, Set5, Set14, BSD100, Urban100, SVT, and CelebA-HQ datasets. No augmentations, random scaling, or patch extraction were applied. The full high-resolution images were passed through each network as a set of coordinates to obtain the upscaled RGB pixel values.

A.2 Model specifications

Table 2 presents details about the parameter counts and memory requirements for each model and encoder used in the empirical study, consistent with previously reported specifications [17]. Both EDSR and RDN encoders produce latent feature maps of size $(B, 64, H, W)$, where 64 is the channel dimension, HW corresponds to the input

Model	Parameters (in million)	Memory (GB)
MetaSR	0.45	1.2
LIIF	0.35	1.3
LTE	0.49	1.4
SRNO	0.81	7.1
CiaoSR	1.43	12.6
HIIF	1.33	1.5
EDSR	1.5	2.2
RDN	21.9	3.0

Table 2: Parameter counts and memory requirements for INR-based ASSR models and encoders.

patch size, and B is the batch size. The upsampling modules in both encoders were not used. EDSR employs 16 residual blocks, while RDN uses 16 RDB blocks, following conventions from prior INR-based experiments. The decoder architectures were left unchanged from the original works, ensuring a fair comparison across techniques.

A.3 Optimization setup

All models were trained using the Adam optimizer with a starting learning rate of 0.0004 for both SGDR and multi-step schedules. The Adam parameters were set as: $\beta_1 = 0.9$, $\beta_2 = 0.999$, and $\varepsilon = 1e^{-8}$. For the multi-step scheduler, the learning rate was decayed every 25 epochs, while SGDR used 25 warmup epochs and a minimum learning rate of $2e^{-06}$. For the EDSR [13] encoder-based experiments, we selected a batch size of 32, while for RDN [14], we set the batch size to 16.

A.4 Training loss and convergence

All models were trained for 150 epochs, with an additional set of experiments using 100 epochs to examine training cost and scaling behavior. Prior works reported results for 1000 epochs, but we limited the training to 150 epochs to balance computational feasibility and convergence. Figure 8 presents the training loss curves for various models under different configurations, showing that convergence is generally achieved well before 150 epochs, ensuring fair comparisons across models.

B Hybrid pixel-gradient loss

We previously presented an overview of perceptual gains achieved from varying objective designs, demonstrating that the proposed hybrid L1-gradient loss significantly enhances texture preservation in super-resolved images, particularly improving edge and corner fidelity. Here, we provide additional qualitative evaluations comparing our loss against baseline objectives and analyzing the impact of the gradient-weighting factor. Firstly, Table 3 presents the changes in various IQA metrics for the SRNO model with EDSR encoder, as the gradient weighting term in the proposed loss function is increased. The results further confirm that moderate gradient weighting consistently improves texture sharpness, whereas overly large weights lead to degradation in pixel-level reconstruction quality. Figure 9 provides a qualitative comparison between the proposed loss and two baseline objectives. For each method, we additionally visualize the corresponding edge and corner maps, along with the first-order derivative for the same image patches, to highlight differences in texture fidelity and structural detail.

Next, we present Figure 10, which shows the edge and corner maps for the same generated image under different values of λ , illustrating the influence of the gradient weighting term. As observed, increasing λ enhances the sharpness and improves edge and corner retention, indicating stronger texture emphasis, consistent with our earlier quantitative observations.

To further examine texture retention at the feature level, we extract intermediate latent representations from the EDSR encoder for SRNO and compute channel-wise mean feature maps. Figure 11 presents these maps for baseline losses as well as for varying values of the proposed loss’s gradient weighting term. It can be observed that different objective functions lead to distinct levels of feature smoothness, edge retention, and contrast in the learned representations. Moving left to right, we observe improved structural continuity and sharper texture patterns as λ increases. However, beyond a certain threshold, the feature maps begin to disrupt pixel-level fidelity and harm reconstruction quality.

We further investigate this by computing the Gray-Level Co-Occurrence Matrix (GLCM) [54] for the intermediate encoded latent features and report the extracted statistics in Table 4. The results show that the proposed

hybrid loss with moderate values of λ maintains high contrast and GLCM dissimilarity, while preserving moderate energy and Angular Second Moment (ASM). This behavior indicates that the model retains more pronounced texture cues in the latent space, while still maintaining meaningful structure without overfitting to pixel-level noise.

C Detailed results

This section presents an alternative numeric representation of the results. Table 5 reports the PSNR gains of the best-performing models across different scales on the DIV2K validation set. The maximum gain of 0.35dB was achieved by the SRNO model trained with the EDSR-encoder.

Next, we present a breakdown of the previous rankings of each model across different training configurations. We averaged the performance of each technique across different settings to provide mean scores per IQA metric. The top-performing models were then identified for each metric, scale, dataset, and encoder, and are presented in the Table 6 and 7. Table 6 summarizes the best-performing models for DIV2K, Set5, and Set14, while Table 7 reports the corresponding results for BSD100 and Urban100.

C.1 Domain specific results

The SVT and CelebA-HQ datasets were selected to evaluate the techniques on two targeted domains, i.e., real-scene text and face super-resolution. Similar to the previous tables, aggregated results are reported in Tables 8 and 9, but here the top three models are highlighted for selected IQA metrics across different scales and encoders.

C.2 Bias in IQA reporting: Y-Channel vs. RGB evaluation

In the SISR domain, it is common practice to evaluate PSNR, SSIM, and other IQA metrics on the luminance (Y) channel of the YCbCr representation, rather than directly on the generated RGB image [55, 56]. The supporting rationale behind this is that human perception is more sensitive to luminance variations than to color, and the Cb and Cr channels primarily encode color information, which has less impact on capturing high-frequency

Scale	λ	PSNR	SSIM	GMSD	FSIM	VIF	SR-SIM	LPIPS
2x	0.05	34.3357	0.9991	0.0071	0.9995	0.6204	0.9997	0.0677
	0.075	34.4314	0.9991	0.007	0.9995	0.6234	0.9997	0.0653
	0.1	34.4283	0.9991	0.007	0.9995	0.6245	0.9997	0.0642
	0.3	34.3911	0.9991	0.007	0.9995	0.6217	0.9997	0.0668
3x	0.05	30.6622	0.9976	0.038	0.9983	0.5055	0.9991	0.1471
	0.075	30.7503	0.9976	0.0373	0.9983	0.5084	0.9991	0.1417
	0.1	30.7406	0.9977	0.0373	0.9983	0.5092	0.9991	0.1425
	0.3	30.718	0.9976	0.0375	0.9983	0.5073	0.9991	0.1435
4x	0.05	28.7522	0.9924	0.0703	0.9955	0.4284	0.9978	0.2155
	0.075	28.8380	0.9925	0.0692	0.9955	0.4317	0.9978	0.2091
	0.1	28.8297	0.9925	0.0691	0.9956	0.4324	0.9978	0.2107
	0.3	28.8053	0.9925	0.0695	0.9955	0.4303	0.9978	0.2128

Table 3: Impact of varying λ term on different IQA metrics. The best and second-best results are colored red and blue, respectively.

Loss	Contrast	Dissimilarity	Energy	Correlation	ASM	Scale	Best Model	Second Best Model	Gain in PSNR (dB)
L1-Loss	1700	31	0.0155	0.0773	0.0002		EDSR-encoder		
Gram-L1-Loss	1696	30	0.0163	0.0598	0.0003	2	SRNO	HIIF	0.027
Gradient Loss (λ : 0.05)	1840	30	0.0167	0.0189	0.0003	3	SRNO	LTE	0.026
Gradient Loss (λ : 0.075)	1947	32	0.0153	0.0591	0.0002	4	SRNO	CiaoSR	0.035
Gradient Loss (λ : 0.1)	2024	32	0.0153	0.0685	0.0002	6	SRNO	CiaoSR	0.007
Gradient Loss (λ : 0.3)	1565	29	0.0153	0.3020	0.0002	12	SRNO	CiaoSR	0.007
						18	SRNO	CiaoSR	0.015
						24	SRNO	LTE	0.014
						30	SRNO	LTE	0.009
							RDN-encoder		
						2	SRNO	LTE	0.020
						3	SRNO	LTE	0.014
						4	SRNO	CiaoSR	0.022
						6	CiaoSR	SRNO	0.004
						12	SRNO	CiaoSR	0.001
						18	CiaoSR	SRNO	0.002
						24	SRNO	LTE	0.012
						30	SRNO	LTE	0.016

Table 4: Texture descriptor statistics from EDSR-SRNO encoder feature maps trained with various loss functions.

details in the super-resolved image. Prior works report PSNR for benchmark datasets, Set5, Set14, BSD100, and Urban100, using only the Y-channel, while DIV2K results are typically reported on RGB images [17, 11, 12]. We followed the same convention in all the results presented before. However, to further investigate the impact of this evaluation choice, an additional analysis was conducted comparing IQA metrics computed on the full RGB image versus the Y-channel alone. For each model trained under various settings, results were averaged separately for RGB- and Y-channel-based evaluations across different IQA metrics, scales, and benchmark datasets. Figures 12 and 13 report the performance gains observed when computing metrics on the Y-channel alone compared to the full RGB image.

The analysis reveals a consistent increase in reported performance when using the Y-channel alone compared to the full RGB image. This highlights an important source

of bias in evaluation that, while commonly applied in prior works, is rarely discussed in detail. Note that LPIPS and FSIM are excluded from this comparison, as they are always computed on RGB images and cannot be meaningfully applied to the Y-channel alone.

Table 5: PSNR gains of the best-performing models at various scales for EDSR and RDN-based encoders. The largest gain for each encoder is highlighted in bold.

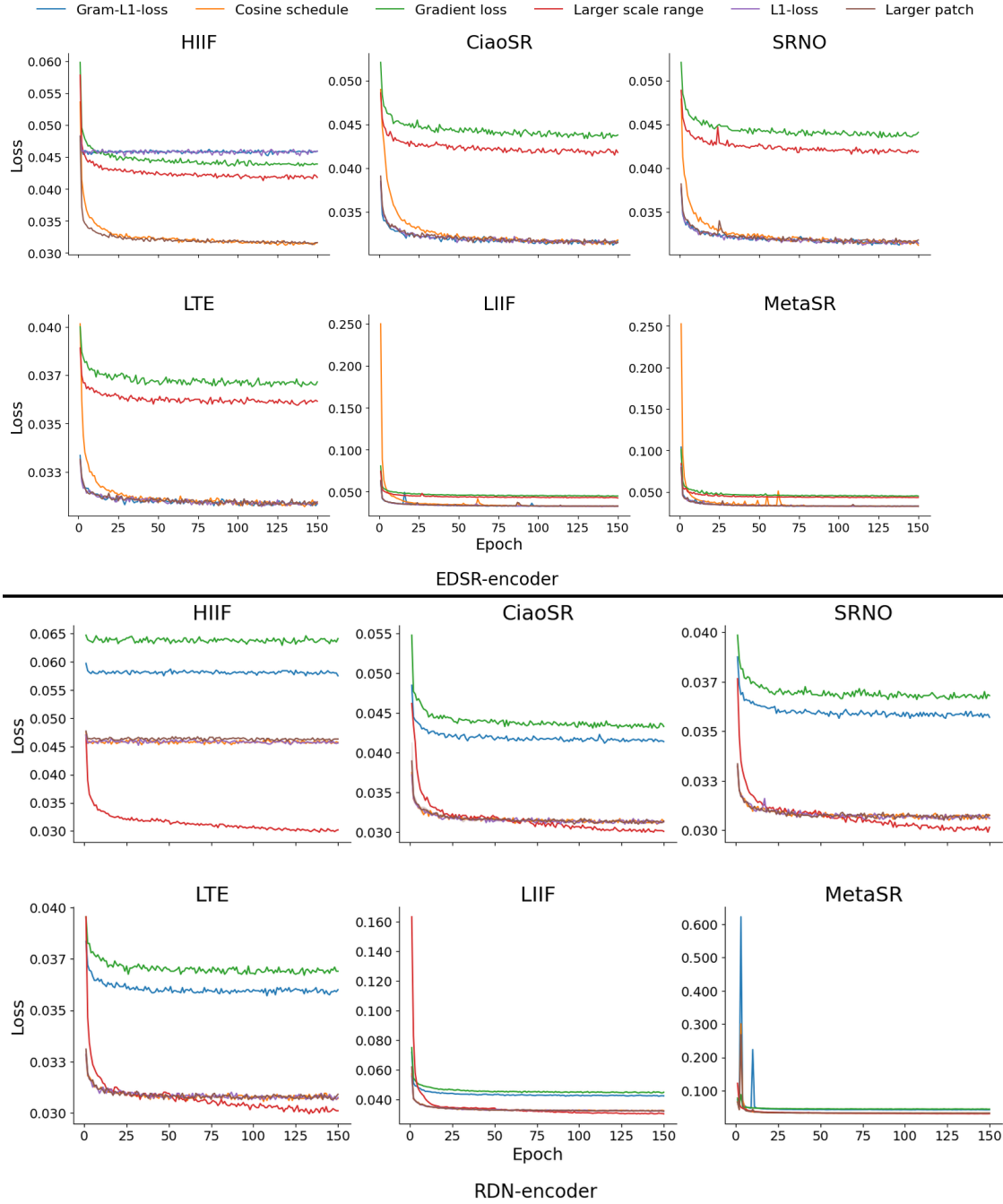


Figure 8: Training losses plotted against the epochs for different techniques trained under different settings. All achieved convergence way before 150 epochs.

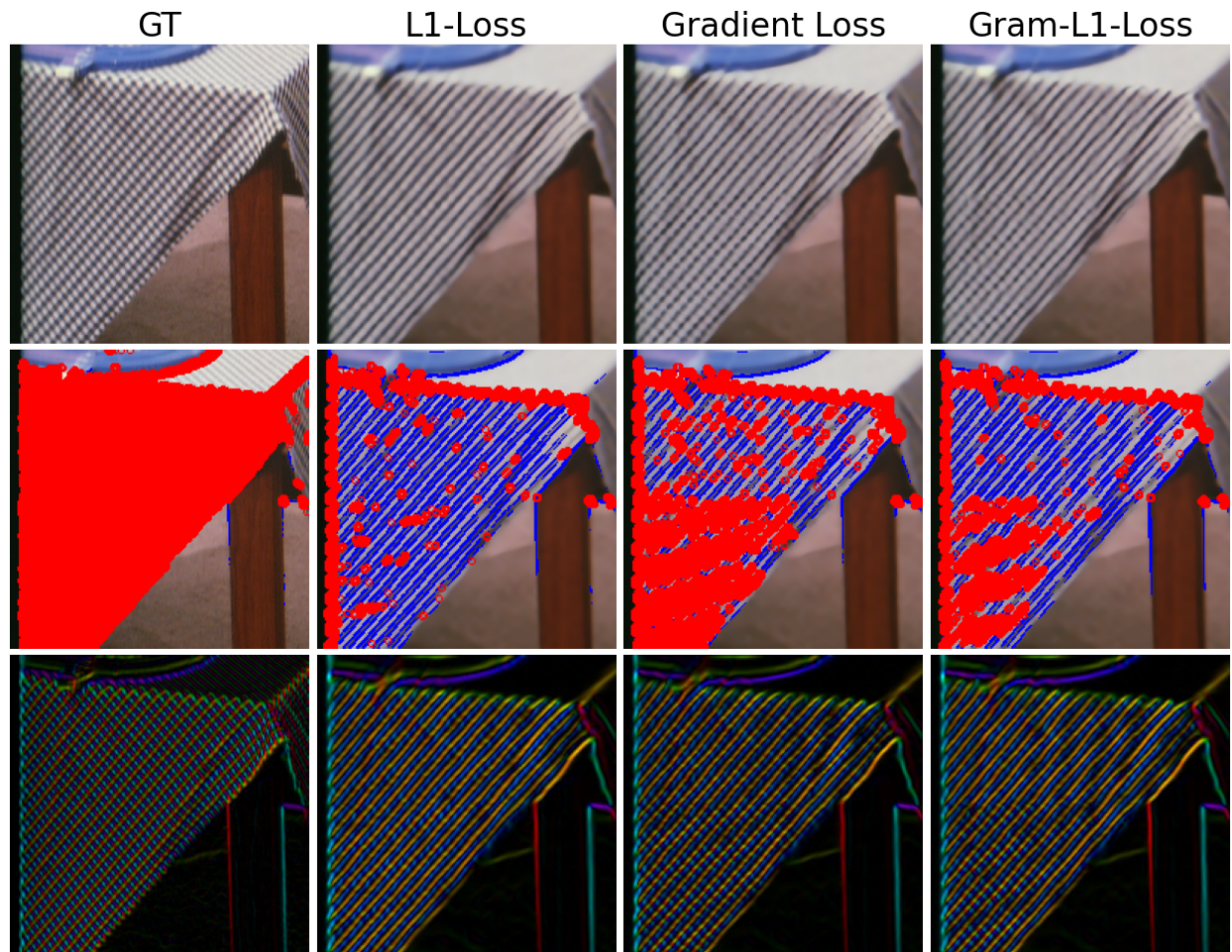


Figure 9: First order derivative, and edge-corner maps for the SRNO model trained with different loss functions on a Set14 image (scaled 4.5x). The Gradient Loss produces sharper edges and corners.

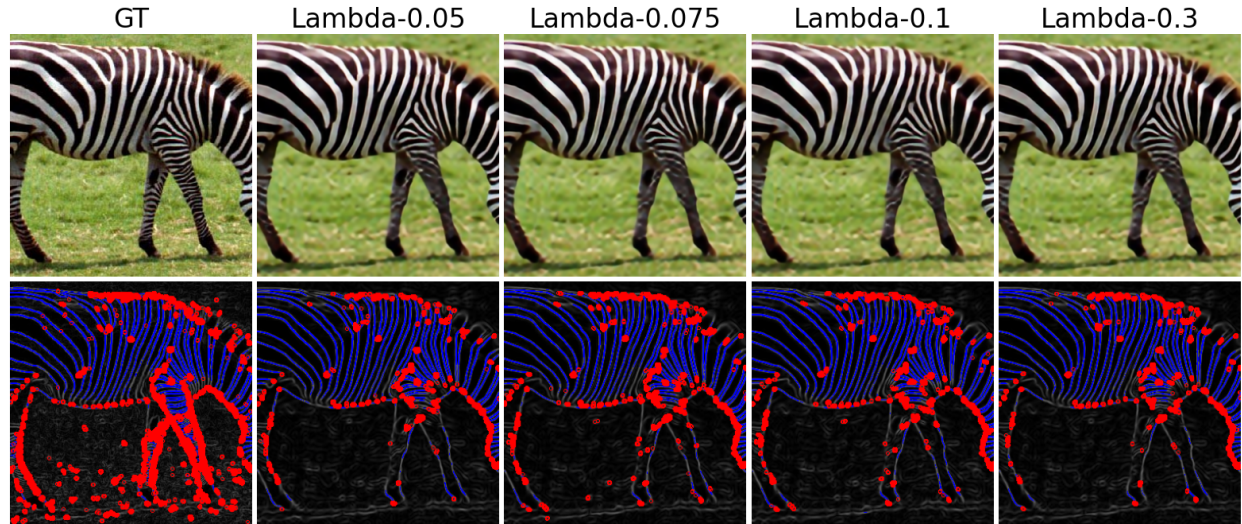


Figure 10: Edge/corner map for image selected from Set14 scaled to 4.5x. A general increase in corners and edges is extracted as the lambda is increased.

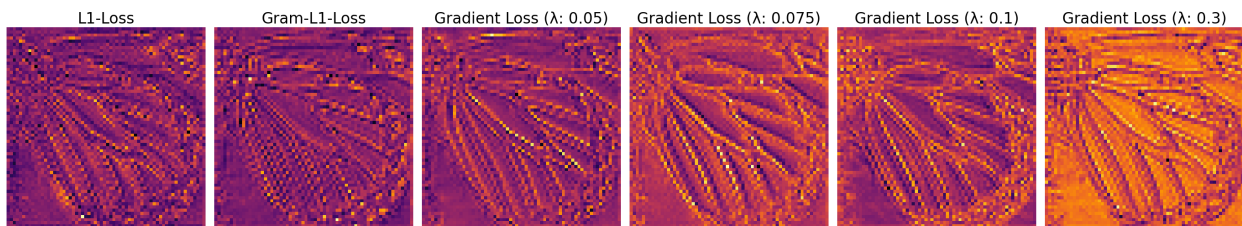


Figure 11: Feature maps extracted from the EDSR encoder of the SRNO model, trained using different loss functions.

Scale	PSNR	SSIM	GMSD	FSIM	VIF	SR-SIM	LPIPS
DIV2K							
EDSR-encoder							
2	SRNO: 34.4143	LTE: 0.9991	LTE: 0.0069	LTE: 0.9995	SRNO: 0.6229	LTE: 0.9997	CiaoSR: 0.0643
3	SRNO: 30.7396	LTE: 0.9976	SRNO: 0.0374	LTE: 0.9983	LTE: 0.5084	MetaSR: 0.9991	CiaoSR: 0.1407
4	CiaoSR: 28.8297	SRNO: 0.9924	SRNO: 0.0694	SRNO: 0.9955	CiaoSR: 0.4318	SRNO: 0.9978	CiaoSR: 0.2085
6	CiaoSR: 26.6362	SRNO: 0.9758	SRNO: 0.1219	LTE: 0.9894	CiaoSR: 0.3201	SRNO: 0.9939	CiaoSR: 0.3263
12	CiaoSR: 23.6416	SRNO: 0.8781	SRNO: 0.1991	SRNO: 0.929	CiaoSR: 0.1673	SRNO: 0.9596	CiaoSR: 0.5384
18	SRNO: 22.1178	SRNO: 0.7766	MetaSR: 0.2326	SRNO: 0.8613	SRNO: 0.1124	SRNO: 0.9196	CiaoSR: 0.6187
24	SRNO: 21.1366	SRNO: 0.6898	MetaSR: 0.2521	CiaoSR: 0.8045	SRNO: 0.0854	SRNO: 0.8832	SRNO: 0.6556
30	SRNO: 20.4501	SRNO: 0.6253	CiaoSR: 0.2645	SRNO: 0.7592	SRNO: 0.07	SRNO: 0.8452	SRNO: 0.6718
RDN-encoder							
2	SRNO: 34.5854	LTE: 0.9992	LTE: 0.0066	LTE: 0.9995	SRNO: 0.6278	LTE: 0.9997	SRNO: 0.0629
3	LTE: 30.8858	LTE: 0.9977	LTE: 0.0361	LTE: 0.9984	LTE: 0.5141	LTE: 0.9991	CiaoSR: 0.1384
4	SRNO: 28.9513	LTE: 0.9927	SRNO: 0.0675	LTE: 0.9957	LTE: 0.4368	LTE: 0.9979	CiaoSR: 0.2051
6	CiaoSR: 26.7378	SRNO: 0.9767	SRNO: 0.1196	LTE: 0.9899	CiaoSR: 0.325	LTE: 0.9941	LIIF: 0.321
12	CiaoSR: 23.7185	SRNO: 0.8811	SRNO: 0.1972	SRNO: 0.9314	CiaoSR: 0.1707	SRNO: 0.961	LIIF: 0.5283
18	SRNO: 22.1842	CiaoSR: 0.7808	CiaoSR: 0.2318	SRNO: 0.8644	SRNO: 0.1149	SRNO: 0.9214	LIIF: 0.6091
24	SRNO: 21.1929	SRNO: 0.6947	CiaoSR: 0.2513	CiaoSR: 0.808	LTE: 0.0872	CiaoSR: 0.8855	LIIF: 0.6497
30	SRNO: 20.4974	SRNO: 0.6297	CiaoSR: 0.2636	SRNO: 0.7626	LTE: 0.0714	SRNO: 0.8474	SRNO: 0.6698
Set5							
EDSR-encoder							
2	SRNO: 37.813	LTE: 0.9661	LTE: 0.0021	SRNO: 0.9789	SRNO: 0.7261	SRNO: 0.991	CiaoSR: 0.0535
3	SRNO: 34.1995	LTE: 0.9355	LTE: 0.0188	LTE: 0.9518	LTE: 0.6284	SRNO: 0.978	LIIF: 0.1122
4	CiaoSR: 32.0539	CiaoSR: 0.9056	SRNO: 0.0439	CiaoSR: 0.9273	CiaoSR: 0.555	SRNO: 0.9658	MetaSR: 0.1531
6	SRNO: 28.7492	SRNO: 0.8393	SRNO: 0.0963	SRNO: 0.8761	SRNO: 0.4259	SRNO: 0.9297	SRNO: 0.2394
8	LTE: 26.7686	SRNO: 0.7765	SRNO: 0.1388	SRNO: 0.828	SRNO: 0.3324	SRNO: 0.8924	SRNO: 0.3169
12	SRNO: 24.5048	SRNO: 0.6882	SRNO: 0.1941	SRNO: 0.7631	SRNO: 0.2263	MetaSR: 0.8366	SRNO: 0.4316
RDN-encoder							
2	LTE: 37.9457	SRNO: 0.9665	LTE: 0.002	SRNO: 0.9795	LTE: 0.7292	SRNO: 0.9913	SRNO: 0.0527
3	LTE: 34.3437	LTE: 0.9369	SRNO: 0.0182	LTE: 0.9532	LTE: 0.6331	SRNO: 0.9787	LIIF: 0.1115
4	CiaoSR: 32.1847	LTE: 0.9075	LTE: 0.0425	CiaoSR: 0.9292	LTE: 0.5605	SRNO: 0.9669	SRNO: 0.1528
6	SRNO: 28.8677	LTE: 0.8422	SRNO: 0.0942	SRNO: 0.8781	LTE: 0.4327	LTE: 0.931	SRNO: 0.2362
8	LTE: 26.9388	LTE: 0.7815	SRNO: 0.1369	LTE: 0.8311	LTE: 0.3413	SRNO: 0.8942	SRNO: 0.3116
12	LTE: 24.5965	LTE: 0.6915	SRNO: 0.1925	LTE: 0.7644	LTE: 0.2312	SRNO: 0.8362	SRNO: 0.4235
Set14							
EDSR-encoder							
2	SRNO: 33.4291	LTE: 0.9691	LTE: 0.0079	LTE: 0.9813	LTE: 0.6102	LTE: 0.9917	CiaoSR: 0.078
3	SRNO: 30.2015	LTE: 0.9073	SRNO: 0.0395	LTE: 0.9491	LTE: 0.5047	LTE: 0.9762	CiaoSR: 0.1657
4	SRNO: 28.4768	CiaoSR: 0.8493	CiaoSR: 0.0714	CiaoSR: 0.9089	LTE: 0.4319	CiaoSR: 0.9563	CiaoSR: 0.2375
6	CiaoSR: 26.314	CiaoSR: 0.7639	LTE: 0.1265	CiaoSR: 0.8433	CiaoSR: 0.3228	CiaoSR: 0.9164	CiaoSR: 0.3659
8	SRNO: 24.8267	SRNO: 0.6989	CiaoSR: 0.1652	CiaoSR: 0.7896	CiaoSR: 0.248	CiaoSR: 0.8813	SRNO: 0.4676
12	SRNO: 23.0719	SRNO: 0.6104	CiaoSR: 0.209	SRNO: 0.7133	LTE: 0.1639	SRNO: 0.8168	SRNO: 0.5713
RDN-encoder							
2	LTE: 33.5897	LTE: 0.9696	LTE: 0.0076	LTE: 0.9819	LTE: 0.6152	LTE: 0.9919	CiaoSR: 0.0768
3	LTE: 30.3271	LTE: 0.9095	LTE: 0.0384	LTE: 0.9504	LTE: 0.5107	LTE: 0.9769	CiaoSR: 0.163
4	SRNO: 28.5864	LTE: 0.8514	LTE: 0.0696	CiaoSR: 0.9107	LTE: 0.4379	CiaoSR: 0.9573	CiaoSR: 0.2349
6	CiaoSR: 26.4213	LTE: 0.7671	CiaoSR: 0.1243	CiaoSR: 0.8463	LTE: 0.3284	CiaoSR: 0.9179	CiaoSR: 0.362
8	CiaoSR: 24.9101	LTE: 0.7026	CiaoSR: 0.163	CiaoSR: 0.7928	LTE: 0.2532	CiaoSR: 0.8824	SRNO: 0.4613
12	LTE: 23.1313	LTE: 0.6144	CiaoSR: 0.2074	LTE: 0.7158	LTE: 0.1679	SRNO: 0.8186	SRNO: 0.5663

Table 6: Top performing model on DIV2K, Set5, and Set14 validation sets, for different scaling factors and different IQA metrics.

Scale	PSNR	SSIM	GMSD	FSIM	VIF	SR-SIM	LPIPS
BSD100							
EDSR-encoder							
2	LTE: 32.0489	LTE: 0.8979	LTE: 0.0087	LTE: 0.9447	LTE: 0.5586	LTE: 0.9716	CiaoSR: 0.084
3	SRNO: 28.9941	LTE: 0.8031	LTE: 0.0461	LTE: 0.88	LTE: 0.4473	LTE: 0.9368	CiaoSR: 0.1877
4	CiaoSR: 27.4932	CiaoSR: 0.7333	LTE: 0.0802	LTE: 0.8261	LTE: 0.373	LTE: 0.9091	CiaoSR: 0.2737
6	CiaoSR: 25.7802	CiaoSR: 0.645	SRNO: 0.1337	CiaoSR: 0.7464	CiaoSR: 0.2703	CiaoSR: 0.8513	CiaoSR: 0.4157
8	SRNO: 24.7348	SRNO: 0.5922	SRNO: 0.1678	CiaoSR: 0.6886	SRNO: 0.2041	CiaoSR: 0.799	SRNO: 0.5431
12	SRNO: 23.4431	SRNO: 0.5376	LIIF: 0.2062	MetaSR: 0.6196	SRNO: 0.1349	MetaSR: 0.7351	SRNO: 0.6639
RDN-encoder							
2	LTE: 32.1524	LTE: 0.8991	LTE: 0.0085	SRNO: 0.9458	LTE: 0.562	LTE: 0.9722	CiaoSR: 0.0828
3	LTE: 29.0817	LTE: 0.8055	LTE: 0.0452	LTE: 0.8817	LTE: 0.4511	LTE: 0.9378	CiaoSR: 0.1855
4	LTE: 27.5659	LTE: 0.7359	LTE: 0.0789	LTE: 0.8283	LTE: 0.3771	LTE: 0.9103	SRNO: 0.2705
6	SRNO: 25.8323	CiaoSR: 0.6473	SRNO: 0.1322	CiaoSR: 0.7488	CiaoSR: 0.2734	CiaoSR: 0.8529	SRNO: 0.4111
8	SRNO: 24.7912	SRNO: 0.5945	SRNO: 0.1662	CiaoSR: 0.6909	SRNO: 0.2073	CiaoSR: 0.8006	SRNO: 0.5361
12	SRNO: 23.4863	SRNO: 0.5393	CiaoSR: 0.2051	SRNO: 0.6209	SRNO: 0.1371	SRNO: 0.7325	SRNO: 0.6588
Urban100							
EDSR-encoder							
2	SRNO: 31.6894	SRNO: 0.9961	SRNO: 0.014	LTE: 0.9971	SRNO: 0.6076	SRNO: 0.9986	CiaoSR: 0.0563
3	CiaoSR: 27.8731	LTE: 0.9909	CiaoSR: 0.0511	LTE: 0.9936	SRNO: 0.4901	LTE: 0.9949	CiaoSR: 0.1254
4	CiaoSR: 25.9269	CiaoSR: 0.9585	CiaoSR: 0.0888	CiaoSR: 0.9812	CiaoSR: 0.4131	CiaoSR: 0.9905	CiaoSR: 0.1918
6	CiaoSR: 23.659	CiaoSR: 0.8948	CiaoSR: 0.1548	CiaoSR: 0.9424	CiaoSR: 0.2978	CiaoSR: 0.9711	CiaoSR: 0.308
8	CiaoSR: 22.3679	CiaoSR: 0.8254	SRNO: 0.1993	CiaoSR: 0.8917	CiaoSR: 0.224	CiaoSR: 0.9439	CiaoSR: 0.4077
12	CiaoSR: 20.8334	CiaoSR: 0.702	MetaSR: 0.2502	CiaoSR: 0.8003	CiaoSR: 0.1398	CiaoSR: 0.8947	CiaoSR: 0.5502
RDN-encoder							
2	LTE: 32.0783	LTE: 0.9964	LTE: 0.013	LTE: 0.9975	LTE: 0.6184	LTE: 0.9987	SRNO: 0.0539
3	LTE: 28.1749	LTE: 0.9917	LTE: 0.0481	LTE: 0.9942	LTE: 0.5025	LTE: 0.9953	CiaoSR: 0.121
4	CiaoSR: 26.1618	LTE: 0.9612	LTE: 0.0848	LTE: 0.9828	LTE: 0.4224	LTE: 0.9912	CiaoSR: 0.1852
6	CiaoSR: 23.8322	LTE: 0.9001	CiaoSR: 0.1502	LTE: 0.9462	CiaoSR: 0.3063	LTE: 0.973	CiaoSR: 0.2977
8	CiaoSR: 22.5116	CiaoSR: 0.833	SRNO: 0.195	SRNO: 0.897	CiaoSR: 0.2316	SRNO: 0.9468	CiaoSR: 0.3955
12	CiaoSR: 20.9493	CiaoSR: 0.7117	CiaoSR: 0.2471	CiaoSR: 0.8074	CiaoSR: 0.1456	CiaoSR: 0.8986	CiaoSR: 0.5382

Table 7: Top performing model on BSD100 and Urban100 validation sets, for different scaling factors and different IQA metrics.

Scale	EDSR-encoder				RDN-encoder			
	PSNR	SSIM	GMSD	VIF	PSNR	SSIM	GMSD	VIF
2	CiaoSR: 39.2331 LIIF: 38.9758 LTE: 37.7051	CiaoSR: 0.9995 LIIF: 0.9988 LTE: 0.9984	CiaoSR: 0.0038 LIIF: 0.004 LTE: 0.0073	CiaoSR: 0.6844 LIIF: 0.681 LTE: 0.6365	SRNO: 39.4012 LTE: 39.3968 CiaoSR: 39.2945	LTE: 0.9996 SRNO: 0.9996 CiaoSR: 0.9996	LTE: 0.0036 SRNO: 0.0036 CiaoSR: 0.0037	SRNO: 0.6895 LTE: 0.6882 CiaoSR: 0.686
3	CiaoSR: 35.8452 LIIF: 35.6992 SRNO: 35.0923	CiaoSR: 0.9967 SRNO: 0.9959 LIIF: 0.9959	CiaoSR: 0.0234 LIIF: 0.0235 SRNO: 0.0259	CiaoSR: 0.5496 LIIF: 0.5468 SRNO: 0.523	SRNO: 35.916 LTE: 35.9146 CiaoSR: 35.8909	LTE: 0.9968 SRNO: 0.9968 CiaoSR: 0.9967	LTE: 0.023 SRNO: 0.023 CiaoSR: 0.0231	LTE: 0.552 SRNO: 0.5518 CiaoSR: 0.551
4	CiaoSR: 34.3028 LIIF: 34.1901 LTE: 34.1168	LTE: 0.9966 SRNO: 0.9965 CiaoSR: 0.9965	CiaoSR: 0.0439 LIIF: 0.0445 LTE: 0.0446	CiaoSR: 0.4742 LIIF: 0.4714 LTE: 0.4685	SRNO: 34.35 LTE: 34.3482 CiaoSR: 34.3402	SRNO: 0.9966 LTE: 0.9966 CiaoSR: 0.9966	SRNO: 0.0433 LTE: 0.0435 CiaoSR: 0.0435	SRNO: 0.4763 LTE: 0.4761 CiaoSR: 0.4758
6	CiaoSR: 32.6996 LTE: 32.6244 SRNO: 32.6226	CiaoSR: 0.9734 LTE: 0.9728 SRNO: 0.9727	CiaoSR: 0.0801 LTE: 0.0803 SRNO: 0.0803	CiaoSR: 0.3777 LTE: 0.3756 LIIF: 0.3752	SRNO: 32.7428 LTE: 32.7385 CiaoSR: 32.7361	SRNO: 0.9738 LTE: 0.9738 CiaoSR: 0.9737	SRNO: 0.0792 LTE: 0.0793 CiaoSR: 0.0797	SRNO: 0.3799 LTE: 0.3798 CiaoSR: 0.3797
8	CiaoSR: 31.7457 SRNO: 31.7124 LTE: 31.7058	CiaoSR: 0.9545 LTE: 0.9544 SRNO: 0.9543	SRNO: 0.1037 CiaoSR: 0.1037 LTE: 0.104	CiaoSR: 0.3183 LTE: 0.3164 SRNO: 0.3161	SRNO: 31.7935 LTE: 31.7856 CiaoSR: 31.7851	SRNO: 0.9552 LTE: 0.9551 CiaoSR: 0.9551	SRNO: 0.1025 LTE: 0.1028 CiaoSR: 0.1032	LTE: 0.3207 SRNO: 0.3206 CiaoSR: 0.3204
12	CiaoSR: 30.4292 SRNO: 30.4262 LTE: 30.4086	CiaoSR: 0.9182 SRNO: 0.9179 LTE: 0.9178	SRNO: 0.1316 CiaoSR: 0.1317 LTE: 0.1325	CiaoSR: 0.2483 SRNO: 0.2477 LTE: 0.2474	CiaoSR: 30.4741 SRNO: 30.473 LTE: 30.4675	CiaoSR: 0.9192 SRNO: 0.9191 LTE: 0.919	SRNO: 0.1306 CiaoSR: 0.1307 LTE: 0.1313	CiaoSR: 0.2505 SRNO: 0.2503 LTE: 0.2503

Table 8: Summary of results achieved on face domain-specific CelebHQ-A dataset.

Scale	EDSR-encoder				RDN-encoder			
	PSNR	SSIM	GMSD	VIF	PSNR	SSIM	GMSD	VIF
2	LIIF: 45.2465 CiaoSR: 44.7078 LTE: 43.0111	CiaoSR: 0.9996 LIIF: 0.9995 LTE: 0.9989	LIIF: 0.0021 CiaoSR: 0.0023 LTE: 0.0058	CiaoSR: 0.8792 LIIF: 0.8738 LTE: 0.8389	CiaoSR: 44.8995 LTE: 44.7038 SRNO: 44.6216	SRNO: 0.9996 LTE: 0.9996 CiaoSR: 0.9996	LTE: 0.0019 CiaoSR: 0.002 SRNO: 0.0021	SRNO: 0.8824 CiaoSR: 0.8809 LTE: 0.8809
3	LIIF: 40.7545 CiaoSR: 40.3483 SRNO: 39.436	CiaoSR: 0.9988 LIIF: 0.9987 SRNO: 0.9986	LIIF: 0.0143 CiaoSR: 0.0145 SRNO: 0.0196	CiaoSR: 0.7833 LIIF: 0.7774 SRNO: 0.744	SRNO: 40.5276 CiaoSR: 40.5019 LTE: 40.4781	SRNO: 0.9989 LTE: 0.9989 CiaoSR: 0.9989	SRNO: 0.0138 LTE: 0.0139 CiaoSR: 0.014	SRNO: 0.7888 LTE: 0.7865 CiaoSR: 0.7864
4	SRNO: 38.0577 LTE: 38.04 LIIF: 38.0388	CiaoSR: 0.9931 LIIF: 0.9927 SRNO: 0.9927	CiaoSR: 0.0354 LIIF: 0.0354 SRNO: 0.0362	CiaoSR: 0.6943 SRNO: 0.6899 LIIF: 0.6889	SRNO: 38.0536 CiaoSR: 37.9505 LTE: 37.9144	SRNO: 0.9935 LTE: 0.9934 CiaoSR: 0.9934	SRNO: 0.0336 CiaoSR: 0.034 LTE: 0.0341	SRNO: 0.7021 CiaoSR: 0.6991 LTE: 0.6983
6	SRNO: 34.4939 LTE: 34.4752 MetaSR: 34.372	SRNO: 0.9704 LTE: 0.9703 CiaoSR: 0.9703	SRNO: 0.078 LTE: 0.0784 MetaSR: 0.0796	SRNO: 0.5384 LTE: 0.5377 CiaoSR: 0.5354	SRNO: 34.5707 LTE: 34.4938 CiaoSR: 34.491	SRNO: 0.9718 CiaoSR: 0.9716 LTE: 0.9715	SRNO: 0.0766 CiaoSR: 0.0773 LTE: 0.0777	SRNO: 0.5458 CiaoSR: 0.5431 CiaoSR: 0.5428
8	SRNO: 32.1595 LTE: 32.1208 CiaoSR: 32.0297	SRNO: 0.9406 LTE: 0.9404 CiaoSR: 0.9403	SRNO: 0.1111 LTE: 0.1117 MetaSR: 0.1123	SRNO: 0.4227 LTE: 0.422 CiaoSR: 0.4211	SRNO: 32.2607 LTE: 32.2203 CiaoSR: 32.2005	SRNO: 0.9431 CiaoSR: 0.9428 LTE: 0.9427	SRNO: 0.1097 CiaoSR: 0.1106 LTE: 0.1107	SRNO: 0.4316 LTE: 0.43 CiaoSR: 0.4294
12	SRNO: 29.3461 CiaoSR: 29.3355 LTE: 29.3089	SRNO: 0.8758 CiaoSR: 0.8758 LTE: 0.8754	MetaSR: 0.1559 SRNO: 0.1562 LTE: 0.1566	CiaoSR: 0.2846 SRNO: 0.2841 LTE: 0.2836	SRNO: 29.4948 CiaoSR: 29.4758 LTE: 29.475	SRNO: 0.88 CiaoSR: 0.8796 CiaoSR: 0.8795	SRNO: 0.1538 LTE: 0.1543 CiaoSR: 0.1545	SRNO: 0.2924 LTE: 0.2918 CiaoSR: 0.2915

Table 9: Summary of results achieved on scene text domain-specific SVT dataset.

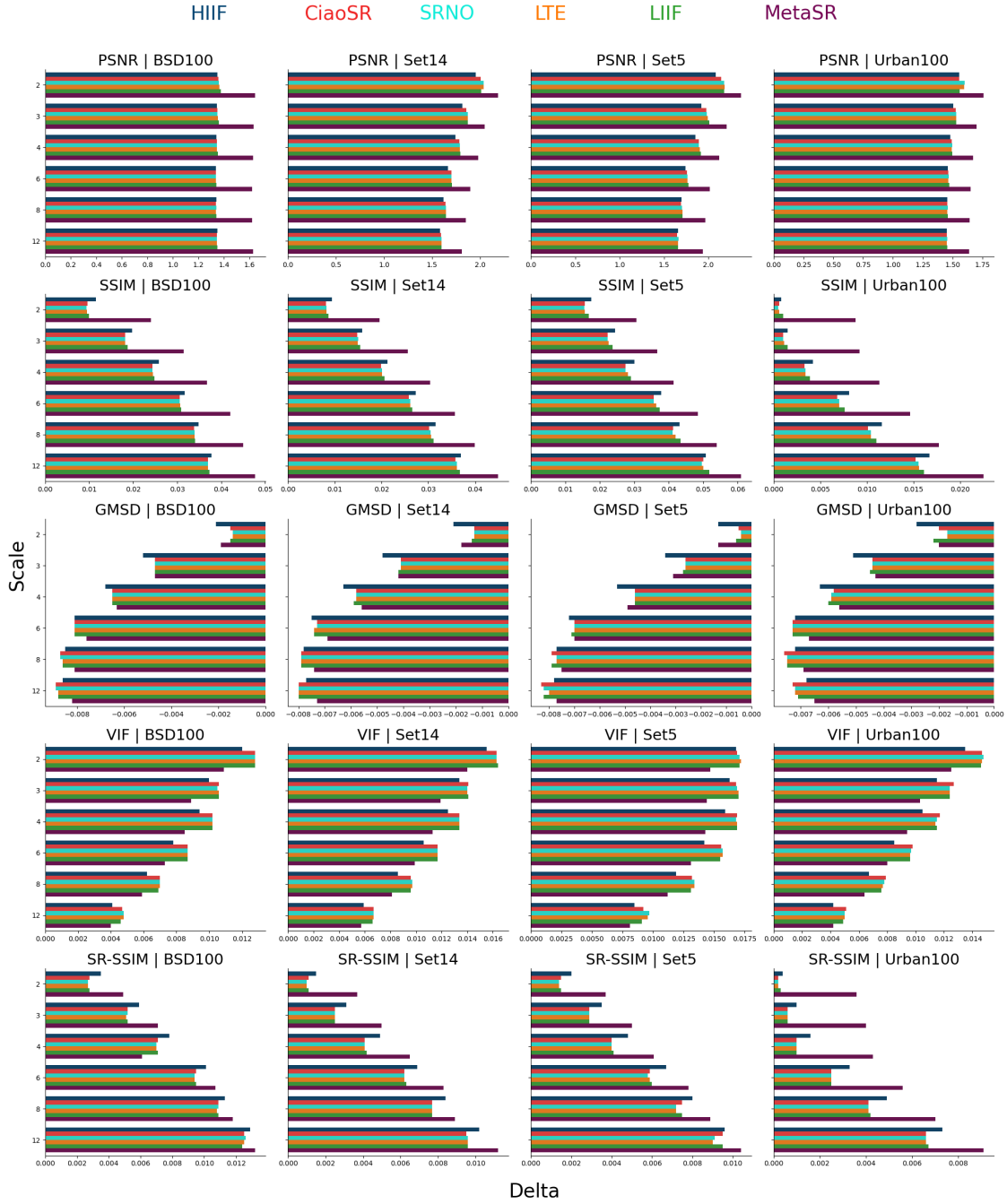


Figure 12: Relative change in IQA when evaluated using the Y-Channel alone for benchmark datasets. EDSR Encoder.

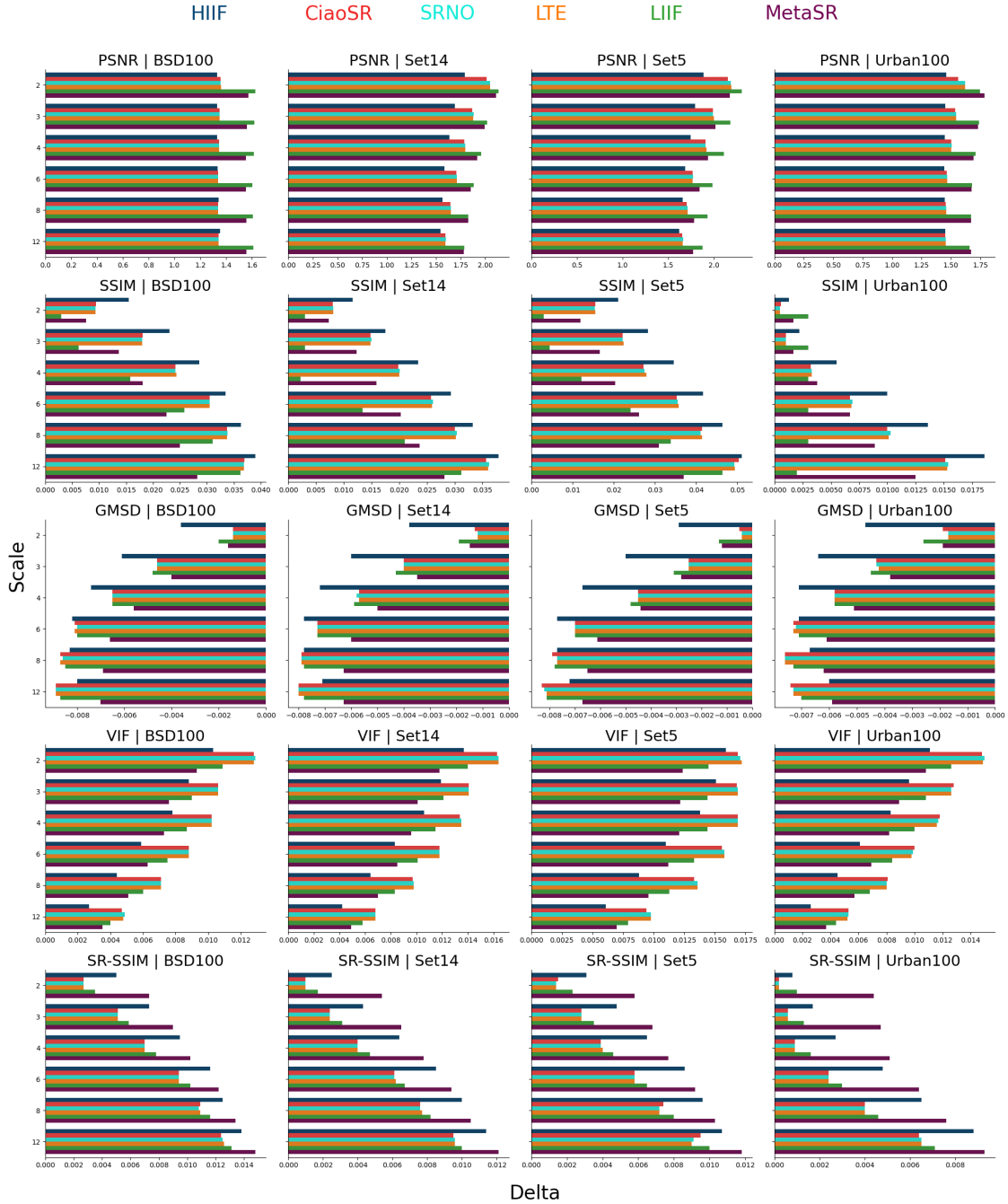


Figure 13: Relative change in IQA when evaluated using the Y-Channel alone for benchmark datasets. RDN Encoder.